chemosensors

Article

Enhanced NO_2 Detection in ZnO-Based FET Sensor: Charge Carrier Confinement in a Quantum Well for Superior Sensitivity and Selectivity

Hicham Helal [1], Marwa Ben Arbia [1,*], Hakimeh Pakdel [1], Dario Zappa [1], Zineb Benamara [2] and Elisabetta Comini [1]

[1] Sensor Lab, Department of Information Engineering, University of Brescia, Via Valotti 9, 25133 Brescia, Italy; hichamwartilani@gmail.com (H.H.); h.pakdel@unibs.it (H.P.); dario.zappa@unibs.it (D.Z.); elisabetta.comini@unibs.it (E.C.)
[2] Laboratoire de Micro-électronique Appliquée, Université Djillali Liabès de Sidi Bel Abbès, Sidi Bel Abbès 22000, Algeria; zbenamara22@gmail.com
* Correspondence: benarbiamarwa94@gmail.com

Abstract

NO_2 is a toxic gas mainly generated by combustion processes, such as vehicle emissions and industrial activities. It is a key contributor to smog, acid rain, ground-level ozone, and particulate matter, all of which pose serious risks to human health and the environment. Conventional resistive gas sensors, typically based on metal oxide semiconductors, detect NO_2 by resistance modulation through surface interactions with the gas. However, they often suffer from low responsiveness and poor selectivity. This study investigates NO_2 detection using nanoporous zinc oxide thin films integrated into a resistor structure and floating-gate field-effect transistor (FGFET). Both Silvaco-Atlas simulations and experimental fabrication were employed to evaluate sensor behavior under NO_2 exposure. The results show that FGFET provides higher sensitivity, faster response times, and improved selectivity compared to resistor-based devices. In particular, FGFET achieves a detection limit as low as 89 ppb, with optimal performance around 400 °C, and maintains stability under varying humidity levels. The enhanced performance arises from quantum well effects at the floating-gate Schottky contact, combined with NO_2 adsorption on the ZnO surface. These interactions extend the depletion region and confine charge carriers, amplifying conductivity modulation in the channel. Overall, the findings demonstrate that FGFET is a promising platform for NO_2 sensors, with strong potential for environmental monitoring and industrial safety applications.

Keywords: FET; nanoporous ZnO; gas sensing; carrier confinement; NO_2 selectivity

check for updates

Received: 9 August 2025
Revised: 22 September 2025
Accepted: 29 September 2025
Published: 1 October 2025

Citation: Helal, H.; Ben Arbia, M.; Pakdel, H.; Zappa, D.; Benamara, Z.; Comini, E. Enhanced NO_2 Detection in ZnO-Based FET Sensor: Charge Carrier Confinement in a Quantum Well for Superior Sensitivity and Selectivity. *Chemosensors* **2025**, *13*, 358. https://doi.org/10.3390/chemosensors13100358

Copyright: © 2025 by the authors. Licensee MDPI, Basel, Switzerland. This article is an open access article distributed under the terms and conditions of the Creative Commons Attribution (CC BY) license (https://creativecommons.org/licenses/by/4.0/).

1. Introduction

Gas sensors are increasingly important across fields such as environmental safety and healthcare. Metal–oxide (MOX) semiconductors are widely studied because they combine high sensitivity and rapid response with [1–3]. Most MOX sensors are implemented in resistor-type designs, valued for their straightforward structure and fabrication. However, the two-terminal configuration restricts their ability to adjust or optimize dynamic behaviors such as response and recovery.

Beyond their use in conventional resistor-type devices, recent research highlights the advantages of integrating MOX into transistor architectures for enhanced gas detection [4].

In particular, field-effect transistor (FET) platforms provide superior control over charge transport and enable modulation of sensing characteristics through biasing schemes or gate engineering. This allows for greater sensitivity, selectivity, and stability compared to traditional two-terminal chemiresistors. Several studies have demonstrated that incorporating MOX such as In_2O_3, WO_3, or ZnO into FET designs leads to significantly improved sensing performance toward toxic gases including NO_2, NH_3, and O_3. For example, Andringa et al. [5] reported a ZnO FET capable of detecting NO_2 down to tens of parts per billion at 200 °C, attributing the response to charge trapping at the dielectric interface. Similarly, Shin et al. [6] showed that WO_3 FETs with floating-gate configurations can exploit charge storage engineering to achieve large improvements in sensitivity and recovery dynamics compared to resistor-type sensors. Their work compares WO_3 chemiresistor and FET gas sensors fabricated on the same wafer. The chemiresistor shows almost constant response across applied voltages, with sensitivity increasing slightly with NO_2 concentration before reaching saturation. Unlike the chemiresistor, the FET device provides greater flexibility because its multi-terminal design allows the use of biasing strategies to adjust performance. By applying charge storage engineering, the FET achieves a much stronger response and higher sensitivity than the resistor device, demonstrating the clear advantage of transistor-based architectures for gas sensing. Recently, Shin et al. [4] developed a FET-type gas sensor by integrating co-sputtered zinc indium tin oxide (ZITO) as the active channel layer. The FET configuration allowed precise modulation of charge transport and facilitated a clear link between surface chemistry and electrical transduction. By varying the ZnO/ITO ratio, they tuned the channel properties, demonstrating that oxygen-vacancy-rich films enhanced NO_2 response at higher operating temperature, while hydroxyl-rich films were more effective at lower temperature. The transistor design was crucial for extracting these differences, as the gate control amplified the sensitivity and provided stability compared to conventional chemiresistors. Their results highlight how material optimization combined with a FET platform can significantly improve detection performance and adaptability of metal-oxide gas sensors.

Recent studies have shown that the morphology of ZnO is a key factor influencing its gas-sensing properties [7,8].

ZnO nanostructures exhibit diverse forms, each tailored for specific gas sensing applications. Among them, the nanoporous variant stands out due to its enhanced surface area and abundance of active sites for gas adsorption. This structure allows for gas diffusion and increases the density of interaction sites, significantly boosting the sensor's sensitivity and responsiveness to target gases. The large surface area of nanoporous ZnO facilitates more effective adsorption and desorption of gas molecules, thereby enhancing the sensor's ability to detect low concentrations. Its nanoscale porosity also contributes to improved catalytic activity and faster response time, making this material well-suited for high-performance gas sensing applications. Y. Nagarjuna et al. [9] have fabricated such a nanoporous structure for a highly efficient ozone gas sensor using a high-power impulse magnetron sputtering process. The sensor demonstrated optimal performance at 200 °C, with a 638% response at 1 ppm O_3, but showed reduced sensitivity as relative humidity increased. They explained this sensing mechanism of the nanoporous ZnO by the adsorption and desorption processes occurring on the material surface. In another study, D. Pleshek et al. [10] have developed highly porous ZnO films using a swelling-assisted sequential infiltration synthesis method based on block copolymer templates. The resulting coatings, with thicknesses ranging from 140 to 420 nm, exhibited up to 98% pore accessibility and presented improved ethanol sensing performance, highlighting their potential for low-temperature sensing applications.

Han et al. [11] developed NH_3 sensors based on organic field-effect transistors (OFETs) using poly (methyl methacrylate) (PMMA) blended with ZnO nanoparticles as the gate

dielectric layer. The ZnO/PMMA hybrid dielectric significantly enhanced sensing performance, showing nearly a tenfold increase in response compared to pure PMMA at 75 ppm NH_3, along with notable shifts in threshold voltage and changes in field-effect mobility. Analysis revealed that the improved sensing was due to the ZnO/PMMA hybrid layer facilitating better interaction between NH_3 and the conducting channel, with the sensors maintaining stability over 40 days in ambient conditions.

Incorporating nanoporous ZnO into various electronic structures and designs significantly enhances its sensitivity in gas-sensing applications. By integrating this nanostructured material into conductometric sensors, Schottky diodes, or field-effect transistors (FETs), the unique surface characteristics of the oxide can be fully exploited.

Such designs enhance catalytic activity and accelerate charge transfer processes resulting in improved selectivity, stability, and response time, making ZnO-based nanosensors more effective in detecting low concentrations of gases in real-time applications.

In this paper, we present the simulation and fabrication of nanoporous ZnO thin-film gas sensors, based on both conventional resistor and Floating Gate Field Effect Transistor (FGFET) structures. This study specifically examines the electron confinement effect within the transistor during the detection of NO_2, aiming to demonstrate its advantages over traditional resistive sensors in terms of sensitivity, response time, and overall performance. Leveraging the gas-sensing properties of ZnO and the advanced functionality of FGFETs, we explore the interaction between NO_2 and the nanoporous oxide surface. To achieve this, we employed Silvaco-Atlas software (Version 3.8.46.R) to simulate the electrical behavior, energy band profiles, and potential diagrams of both sensor types under NO_2 exposure. In the next phase, we plan to experimentally validate the simulation results through the fabrication and testing of the two sensor prototypes.

2. Theoretical Details

2.1. Working Principle of ZnO Sensor

The gas sensing mechanism of ZnO toward NO_2 relies on surface reactions that modify its electrical properties, enabling effective detection.

Initially, when ZnO is exposed to air, oxygen molecules adsorb onto the surface. Depending on the temperature and surface conditions, these adsorbed oxygen are ionized into various ionic species such as O_2^-, O^-, and O^{2-} by the following equations [12].

$$O_2(gas) \rightarrow O_2(ads) \quad (1)$$

$$O_2(ads) + e^- \rightarrow O_2^-(ads) \quad (2)$$

$$O_2^-(ads) + e^- \rightarrow 2O^- \quad (3)$$

$$O^- + e^- \rightarrow O^{2-} \quad (4)$$

Typically, oxygen molecule ions are the dominant species at temperatures up to approximately 150 °C [13]. O^- species prevail between 150–300 °C [14], forming a single electropositive oxygen vacancy V_O^+ [15] and O^{2-} species become dominant at temperatures above 300 °C [16] creating a double electropositive oxygen vacancy V_O^{++} [15] as illustrated in Figure 1 [17]. This process of the extraction of electrons from the surface of the porous ZnO results in the formation of an electron depletion layer near the surface.

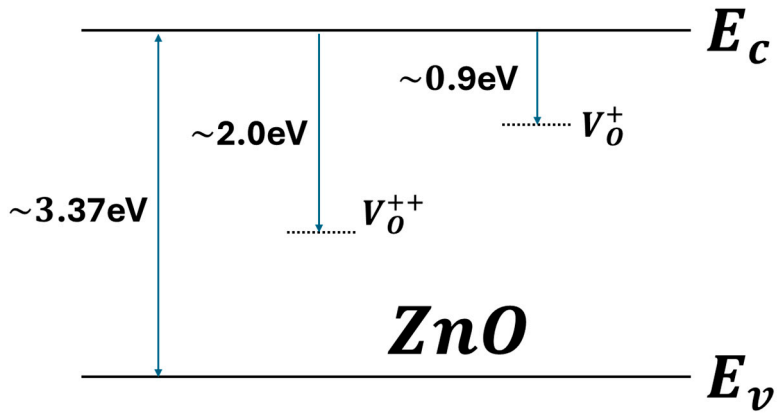


Figure 1. Energy band gap of ZnO with energy levels of oxygen vacancies V_O^+ and V_O^{++}.

When NO_2 gas is introduced, it can either directly adsorb onto the surface of the gas sensor or react with the pre-adsorbed oxygen species [18–20], as described by the following reactions:

$$NO_2 + e^- \rightarrow NO_2^- \quad (5)$$

$$NO_2 + O^- \rightarrow NO_2^- + \frac{1}{2}O_2 \quad (6)$$

$$NO_2^- + O^- \rightarrow 2O^{2-} + NO_2 \quad (7)$$

These reactions further reduce the electron concentration at the ZnO surface, causing the depletion region to extend deeper into the material and increasing the resistance of the sensor, as the conductive path for the electron current becomes narrower.

2.2. Modeling Gas Diffusion and Surface Kinetics in Porous ZnO

The overall sensor response is affected by both surface reaction and gas diffusion rates. The rate of gas diffusion is determined by the microstructure of the sensing layer, the size of the target gas molecules, and Knudsen diffusion.

The Knudsen diffusion coefficient is expressed as [21,22]:

$$D_k = \left(\frac{4r}{3}\right)\left(\frac{2RT}{\pi M}\right)^{\frac{1}{2}} \quad (8)$$

where:

T: temperature.

r: pore radius.

M: molecular mass of the gas molecules.

$R = 8.314$ J.mol^{-1}.K^{-1}: gas constant.

Sakai et al. [23] modeled the gas concentration in relation to the sensing porous film thickness deposited on a substrate using the following diffusion-reaction equation:

$$\frac{\partial C_A}{\partial t} = D_k \frac{\partial^2 C_A}{\partial x^2} - kC_A \quad (9)$$

where:

C_A: concentration of the diffusing/reacting gas.

t: time.

x: spatial coordinate (along diffusion direction).

k: surface reaction rate.

D_k: diffusion coefficient.

The equation applies considering that the diffusion follows the Knudsen mechanism. The gas concentration profile is derived by solving the equation assuming steady-state conditions ($\partial C_A/\partial t = 0$), which depends on the film thickness, surface reaction rate, and diffusion coefficient, obtaining the following equation.

$$C_A = C_{A,S}\frac{\cosh((L-x)\times m)}{\cosh(L\times m)} \tag{10}$$

where:

$C_{A,S}$: concentration of the gas at the surface.

L: film thickness.

$m = \sqrt{\frac{k}{D_k}}$: the reaction-diffusion parameter that represents how strongly the reaction rate dominates over diffusion (it is also defined as the inverse characteristic diffusion length).

Using Sakai et al. model, a simulation of gas concentration within a porous film of 200 nm-thickness deposited on a substrate (Figure 2a) was performed for gas flow of 5 ppm, at different m values (Figure 2b). As can be seen in Figure 2b, the gas concentrations decrease exponentially with the depth from the surface. This decrease accelerates at higher m values indicating that most reactions between the gas and the sensing layer occur close to the surface.

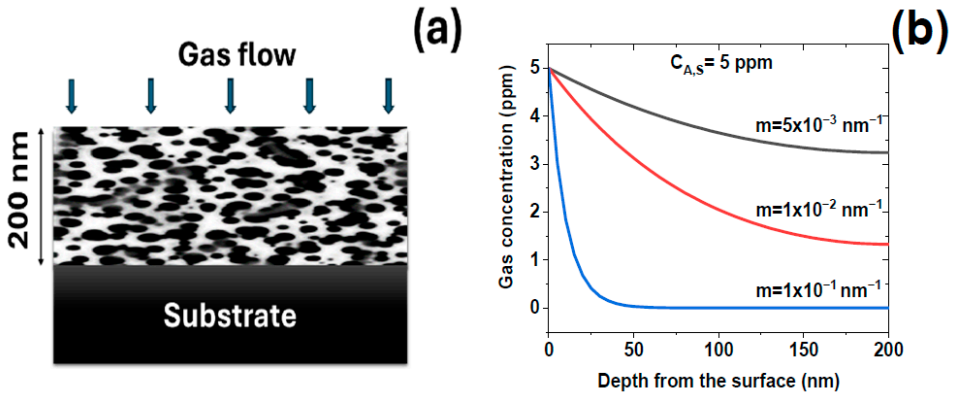


Figure 2. (**a**) Schematic illustration of a porous thin film exposed to gas flow. (**b**) Simulated Gas diffusion profile across sensing layer depth at different m values.

Based on the above results, Silvaco-Atlas software was used to simulate FGFET and conventional resistor gas sensors incorporating a 200 nm ZnO thin film, by taking into consideration the gas behavior of m = 1×10^{-2} nm^{-1} . This value of m was estimated as an intermediate representative parameter, chosen to avoid bias toward either slow or fast diffusion limits. This parameter serves as an illustrative example to study the effect of charge-carrier confinement in a quantum well. It is not intended to represent an exact physical value but rather to emphasize the confinement effects. Silvaco-Atlas is a versatile tool for simulating and analyzing semiconductor devices and integrated circuits. It provides a comprehensive framework for modeling diverse devices using fundamental equations, including Poisson's equation and the continuity equations for electron and hole transport.

The Poisson equation, which describes the relationship between the electrostatic potential and the spatial charge density, is expressed as:

$$\mathrm{div}(\varepsilon\nabla\psi) = -\rho \tag{11}$$

where ψ represents the electrostatic potential, ε denotes the permittivity, and ρ is the space charge density.

The continuity equations for electron and hole carriers are given by [24]:

$$\frac{\partial n}{\partial t} = \frac{1}{q} div\ j_n + g_n - r_n \tag{12}$$

$$\frac{\partial p}{\partial t} = -\frac{1}{q} div\ j_p + g_p - r_p \tag{13}$$

where n and p are the electron and hole concentrations, j_n and j_p are the electron and hole current densities, g_n and g_p are the generation rates for electrons and holes, r_n and r_p are the recombination rates for electrons and holes, and q is the elementary electric charge.

Equations (11)–(13) provide the general framework for device simulation. However, Silvaco-Atlas also includes additional secondary equations to describe specific physical models for parameters like g_n, r_n, g_p, and r_p. The current density equations, or charge transport models, are typically obtained by applying approximations and simplifications to the Boltzmann transport equation. Depending on the assumptions, different transport models can be derived, including the drift-diffusion, energy balance transport, and hydrodynamic models [25].

Several physical models are implemented in the simulations. These include the Shockley–Read–Hall (SRH) recombination and Auger recombination rate models to account for trap-assisted tunneling and the minority recombination effects, Lombardi CVT model for electric field-, temperature-, and concentration-dependent mobility calculations, Fermi Dirac statistics for carrier distribution, FLDMOB to describe mobility under lateral electric field, and CONSRH (a defect-free SRH recombination model) for bandgaps.

Additionally, the effect of NO_2 gas is incorporated by introducing the density of states (DOS) within the bandgap that act as electron acceptors. These states capture electrons from the conduction band, thereby altering the sensor's electronic properties [26–28], as illustrated in Figure 1.

The DOS is composed of four bands: two tail bands (a donor-like valence band $g_{TD}(E)$ and an acceptor-like conduction band $g_{TA}(E)$), modeled using an exponential distribution, and two deep-level bands (one donor-like $g_{GD}(E)$ and one acceptor-like $g_{GA}(E)$), modeled using a Gaussian distribution. This can be expressed as follows [25]:

$$g_{TA}(E) = N_{TA}\ exp\left(\frac{E - E_c}{\omega_{TA}}\right) \tag{14}$$

$$g_{TD}(E) = N_{TD}\ exp\left(\frac{E_v - E}{\omega_{TD}}\right) \tag{15}$$

$$g_{GA}(E) = N_{GA}\ exp\left[-\left(\frac{E_{GA} - E}{\omega_{GA}}\right)^2\right] \tag{16}$$

$$g_{GD}(E) = N_{GD}\ exp\left[-\left(\frac{E - E_{GD}}{\omega_{GD}}\right)^2\right] \tag{17}$$

where E represents the trap energy, E_c denotes the conduction band energy, E_v refers to the valence band energy, and ω symbolizes the characteristic decay energy. The subscripts T, G, A, and D correspond to tail states, Gaussian (deep level) states, acceptor states, and donor states, respectively.

Figure 3a,b show the device architectures of the conventional resistive gas sensor and the FGFET-based gas sensor, respectively. Both configurations use a 200 nm-thick n-type ZnO sensing layer, with an intrinsic charge carrier concentration of 5×10^{17} cm^{-3}. The two sensor structures share a common layout featuring a pair of top-deposited ohmic contacts, each 1 µm thick and 600 nm wide, spaced 600 nm apart on the ZnO surface.

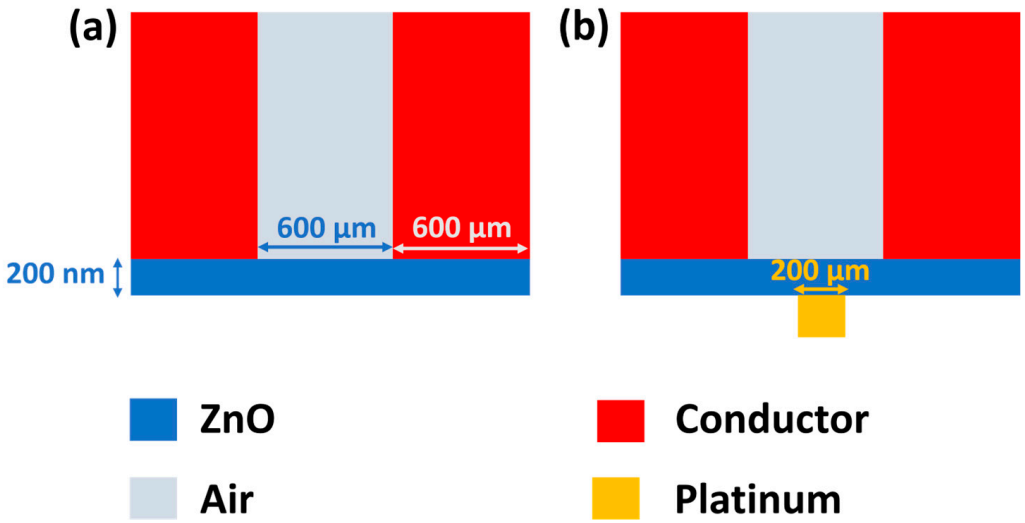


Figure 3. Graphic structure of the resistor (**a**) and FGFET (**b**) based gas sensors.

In the FGFET design, a Schottky gate electrode made of platinum (Pt) is integrated beneath the ZnO layer. This gate is 100 nm thick and 200 µm wide. Additionally, an air gap is defined above the ZnO film, between the two ohmic contacts, to simulate the gas exposure environment.

During the simulation, Silvaco-Atlas assigns relevant physical and electrical properties to each material involved, including parameters such as bandgap energy, electron affinity, dielectric permittivity, and carrier mobility. These material-specific parameters are crucial for accurately modeling the electrical response and overall performance of the gas sensing devices.

3. Experimental Details

3.1. Fabrication Process

The FGFET and resistive gas sensor structures were fabricated following the simulation designs. Alumina (Al_2O_3) substrates (2 mm × 2 mm, 2N purity, Kyocera, Japan) were first cleaned ultrasonically in acetone for 20 min, rinsed with ethanol, and dried in synthetic air. For the FGFET structure, a 100 nm-thick Pt layer was deposited on the alumina substrate as a gate Schottky contact using DC magnetron sputtering. A 200 nm-thick Zn layer was then deposited on both sensor structures using the same method. The samples are oxidized at 500 °C for 1 h under a partial vacuum of 0.7 mbar, with a gas flow of 20 sccm O_2 and 80 sccm Ar, resulting in the formation of nanoporous ZnO material. To form the ohmic electrodes, a 50 nm TiW layer followed by 1 µm of Pt was deposited using DC magnetron sputtering at 300 °C, ensuring strong adhesion to the alumina substrates. The TiW layer provided excellent ohmic contact while enhancing adhesion. On the backside of the samples, a 50 nm TiW adhesion layer is deposited, followed by a 1.5 µm-thick Pt heating element, also using DC magnetron sputtering (see Figure 4).

The samples were wire-bonded onto transistor outline (TO) packages using gold wires to form the sensing devices, labeled as 'R' for the resistor sensor and 'TR' for the FGFET sensor. The sensors were stabilized by aging at 450 °C for 48 h. Figure 5 illustrates the main steps in the fabrication process, from the deposition of the metallic layer to the sensors' final readiness for gas testing.

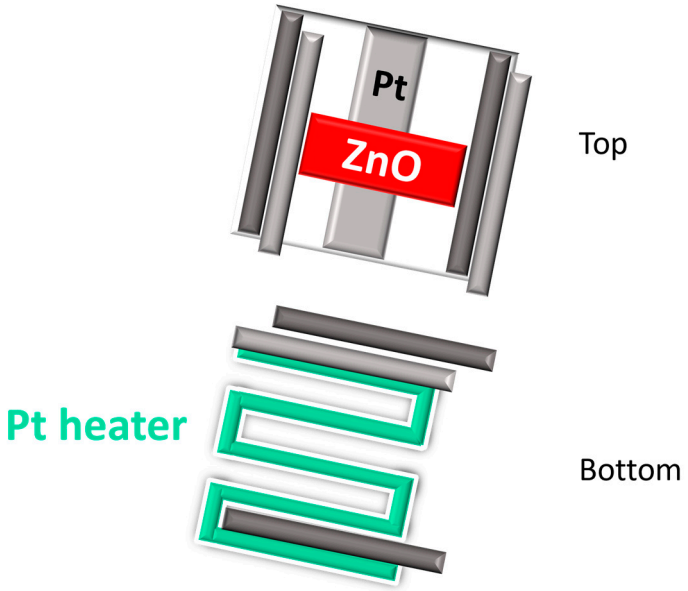


Figure 4. Top and bottom view of the sensor configuration (Transistor).

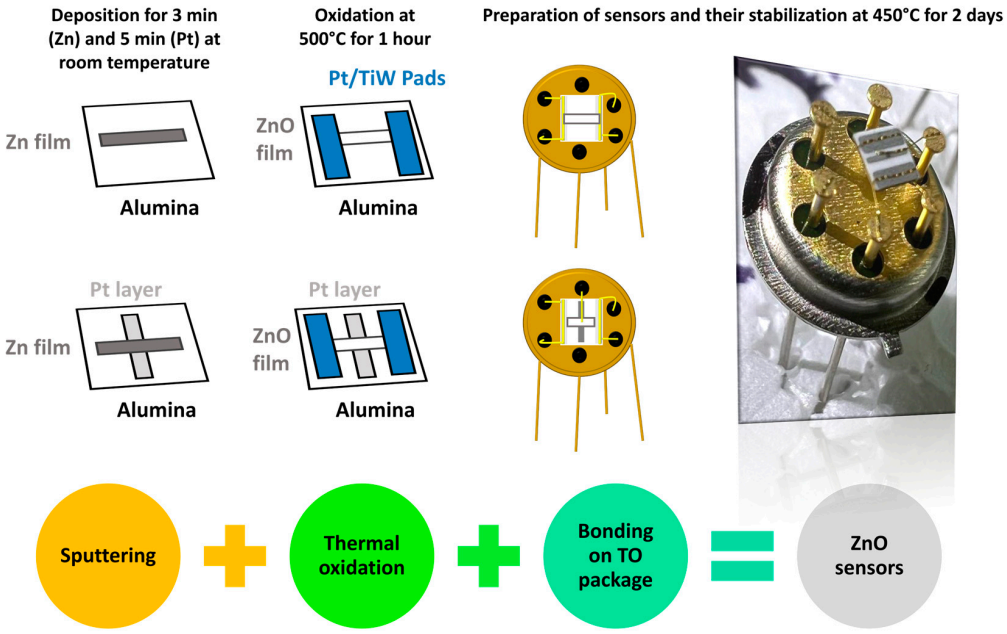


Figure 5. Schematic illustration of sensors' fabrication.

3.2. Characterizations

The morphology of the ZnO sensing layers was characterized using a scanning electron microscope (SEM) with high-resolution (MIRA3 FEG-SEM, TESCAN). The images were captured at 7 kV, with a working distance of 10 mm and magnification of 10,000×.

To assess the gas-sensing performance of the fabricated FGFET and resistive ZnO-based sensors, functional tests were performed inside a stainless-steel climatic chamber (Angelantoni, Massa Martana, Italy, model MTC 120) with a volume of 1 L. This system accommodates up to eight sensors simultaneously, enabling parallel electrical characterization under controlled environmental conditions.

The sensor was mounted on a 6-pin transistor outline (TO) package as shown in Figure 5, although only four pins were used during the measurements:

- Two pins were connected to the platinum heater on the backside of the alumina substrate, ensuring precise thermal control of the device;

- The remaining two pins were connected to the Pt pads on the top ZnO surface for electrical signal measurement.

The TO packages were arranged in the climatic chamber in a consistent configuration, allowing for simultaneous application of heating and real-time conductance monitoring of the active sensing layer.

The target gas concentrations were prepared by diluting certified standard gases (SOL, Italy) with synthetic air using mass flow controllers to obtain the desired levels. The total gas flow was maintained at 200 standard cubic centimeters per minute (sccm) throughout all tests. Each measurement cycle included:

- 30 min of exposure to the target analyte,
- followed by 90 min of synthetic air flow to allow the sensor to return to its baseline conductance.

The electrical response of the sensors was measured by applying a constant voltage ranging from 1 V to 10 V (1 V in our measurement) using an Agilent E3631A DC power supply. The resulting current was continuously monitored using a Keithley 6485 picoammeter, enabling real-time calculation of conductance values.

Sensors were tested toward various oxidizing (e.g., NO_2) and reducing gases (e.g., NH_3, H_2, ethanol) to evaluate selectivity, sensitivity, and repeatability. The relative humidity (RH) inside the chamber was controlled and varied between 0% (dry air) and 80%, to investigate the effect of moisture on sensor response.

All measurements were performed at controlled working temperatures ranging from 150 °C to 400 °C, adjusted using Thurlby Thandar PL330DP power supplies, while the ambient chamber temperature was kept constant at 20 °C. Sensors were preconditioned by thermal aging at 450 °C for 48 h before testing to ensure signal stability and repeatability.

The response ($\frac{\Delta G}{G}$) of each sensor was calculated using the following expressions:

Upon the introduction of the oxidizing (reducing) gas, the response of the devices is calculated as $\frac{\Delta G}{G} = \frac{G_{air} - G_{gas}}{G_{gas}}$ ($\frac{\Delta G}{G} = \frac{G_{gas} - G_{air}}{G_{air}}$).

4. Results and Discussions

4.1. Modelling Results

The simulated current–voltage (I–V) characteristics of the fabricated sensor architectures were obtained using Silvaco-Atlas to assess and compare their electrical responses in the presence and absence of NO_2.

Figure 6a shows the I–V curves extracted from the ohmic contacts of the resistor and FGFET gas sensors, noted R and TR, respectively, with and without the presence of NO_2 gas, at 300 °C.

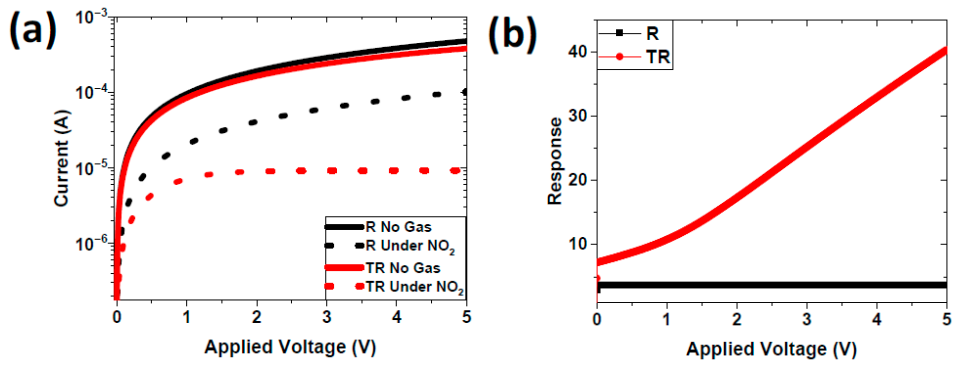


Figure 6. (**a**) Current versus applied voltage before and after exposure to NO_2 and (**b**) gas sensing response of the resistor and FGFET devices toward NO_2.

Both structures display comparable I–V characteristics, with minor deviations at higher voltages likely caused by the gate effect. The current in both cases rises exponentially with increasing applied voltage. Upon exposure to NO_2, both structures show a decrease in the current, with a larger reduction for the FGFET. This occurs because, when the applied voltage exceeds 1.5 V, the current of the FGFET remains nearly constant at approximately 8.85×10^{-6} A, making the reduction more pronounced at higher voltages, unlike the resistor, which exhibits a steady decrease with increasing the applied voltage.

These results demonstrate that the FGFET structure is substantially more sensitive to NO_2 than the resistor sensor. This is further illustrated in Figure 6b, showing the response versus applied voltage calculated as follows,

$$Response = (I_{No\ gas} - I_{Under\ gas})/I_{Under\ gas} \quad (18)$$

The FGFET demonstrates a substantially stronger response to NO_2 than the resistor sensor, and its sensitivity increases with applied voltage, unlike the resistor, which maintains a nearly constant response. The enhanced performance of the FGFET is attributed to its floating gate, which amplifies variations in surface charge induced by NO_2 adsorption on the ZnO layer.

To gain further insight into these effects, the influence of NO_2 on the energy band structure and potential distribution for both sensor configurations is examined in the following section.

Figure 7a,b display the energy band diagram for the resistor and FGFET gas sensors, respectively, highlighting the impact of NO_2 on their energy profiles. At the ZnO/Pt interface, a Schottky barrier with a height of ϕ_b = 1.1 eV and a depletion region with a width of $W_2 = 60$ nm are established. Upon introducing NO_2, significant band bending occurs in both devices as the gas molecules withdraw electrons from the ZnO surface, forming an electron depletion region with a width of $W_1 = 110$ nm. This induces a shift in the conduction and valence band edges (E_c and E_v) by 0.58 eV, resulting in more pronounced bending near the surface.

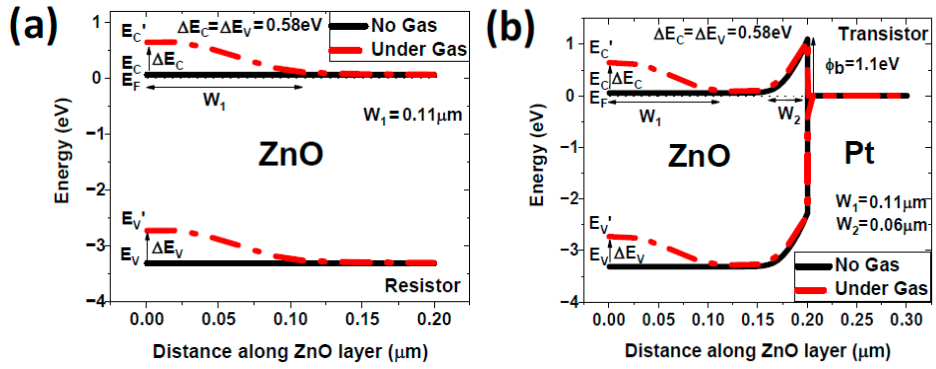


Figure 7. Energy band profile of the (**a**) resistor- and (**b**) FGFET-based gas sensors, along the y-axis.

Furthermore, in the FGFET, the combined effect of the Schottky barrier and band bending generates a quantum well in the conduction channel, which confines charge carriers and amplifies the sensor's response. This quantum well effect enhances the modulation of channel conductivity, rendering the FGFET significantly more sensitive to NO_2 than the resistor-type sensor.

To further analyze this effect, the potential diagrams in Figure 8a,b illustrate the corresponding changes in the electrical potential for the resistor and FGFET gas sensors, respectively. The FGFET structure exhibits a potential barrier of 1.6 V at the interface ZnO/Pt due to the Schottky contact. Upon exposure to NO_2, both structures display

noticeable alterations in their potential profiles. The interaction with NO_2 induces a decrease in the potential, resulting in a potential barrier of 0.6 V for both devices. This change is primarily caused by electron depletion at the ZnO surface, reflecting a reduced free electron concentration due to interactions with NO_2 molecules.

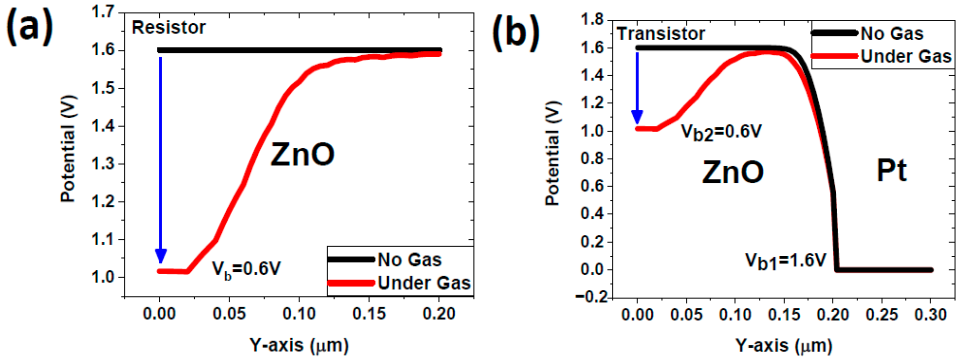


Figure 8. Potential diagram of the resistor (**a**) and FGFET (**b**) based gas sensors, along the y-axis. Blue arrows indicate the potential change after gas exposure.

As a result, the FGFET structure develops two potential barriers under NO_2 exposure, narrowing the conductive channel. This narrowing more effectively restricts the flow of charge carriers compared to the conventional resistor, leading to a greater current reduction, as observed in Figure 6a. This behavior demonstrates that the FGFET architecture provides superior gas sensing performance compared to a standard resistor, making it a more effective choice for detecting gases such as NO_2.

To validate the simulation findings, the FGFET and resistive gas sensor structures were also fabricated and experimentally characterized. The comparison between simulated and measured results allows for a comprehensive understanding of the sensor behavior under NO_2 exposure.

4.2. Experimental Results

The experimental phase focused on reproducing the sensor structures and exposing them to NO_2 gas. By comparing the measured electrical and sensing characteristics with simulation predictions, we aim to validate the enhanced response of the FGFET sensor and its superior sensitivity to NO_2. These experimental results will offer further insights into the practical performance of both sensor architectures, supporting the simulation findings.

The ZnO layer was prepared by sputtering a Zn film onto the alumina substrate, followed by thermal oxidation. The color change from gray (metallic Zn) to transparent after oxidation provided an initial qualitative confirmation of ZnO formation. Furthermore, the cross-bar configuration of the sensor enabled clear observation of the distinct layers using SEM analysis. The SEM image in Figure 9a confirmed the presence and separation of the ZnO and Pt layers, validating the successful formation and integration of the ZnO film.

The ZnO layer exhibits a granular morphology with irregularly distributed grains and well-defined pore boundaries (see Figure 9b,c). Its porous nature and high surface-to-volume ratio make the material particularly suitable for gas sensing, promoting efficient adsorption of gas molecules and effective charge carrier transfer.

The sensors are tested for low concentrations of NO_2 gas at different operating temperatures. Figure 10a,b describe their responses towards 2 ppm and 5 ppm, respectively, showing the highest sensitivities for the FGFET sensors. Unlike the resistor sensor, the TR device exhibits higher responses for NO_2 gas detection at different operating temperatures with optimal performance observed at 400 °C.

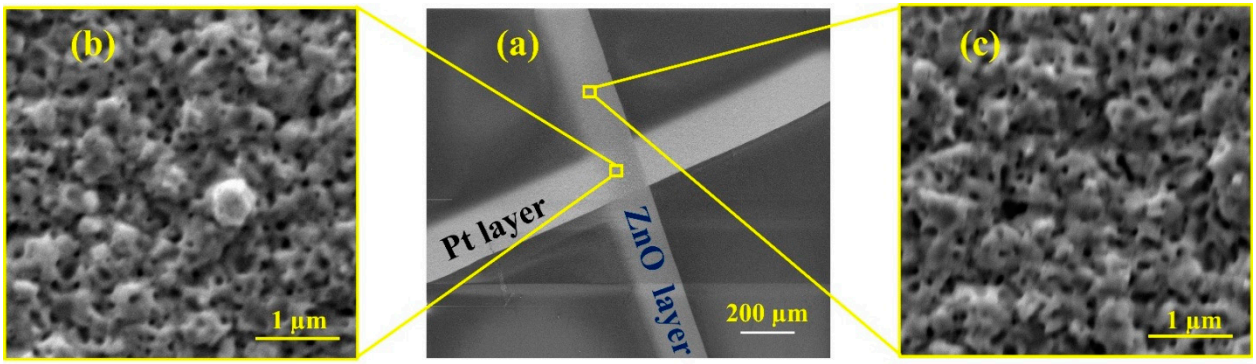


Figure 9. SEM images of ZnO structure (**a**) on Pt (**b**) and on alumina substrate (**c**).

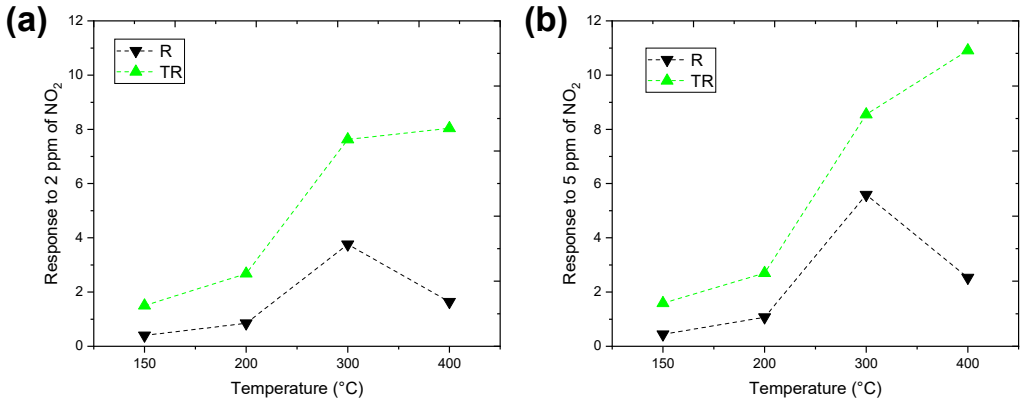


Figure 10. Gas response of the resistor and FGFET sensors at different operating temperatures to (**a**) 2 ppm and (**b**) 5 ppm of NO_2 gas at 40% of relative humidity@20 °C.

The dynamic response and calibration curves of the sensors to NO_2 gas are shown in Figure 11. The observed changes in electrical conductance upon air and gas injection align with the n-type conductivity characteristic of ZnO, as depicted in Figure 11a. Figure 11b shows the calibration performance and sensitivity for R and TR sensors.

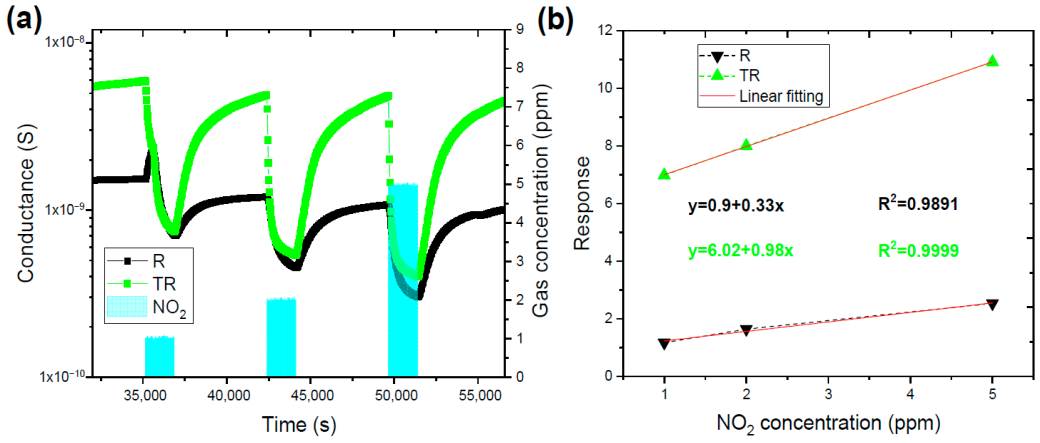


Figure 11. (**a**) The dynamic response-recovery curves of ZnO sensors to 1–5 ppm NO_2 gas at 400 °C and 40% of relative humidity@20 °C. (**b**) The linear fitting curve to relative response in (**a**).

The sensing mechanism of ZnO, before and after exposure to NO_2, is described above in the simulation part. Additionally, the nanoporous morphology of ZnO further enhances the gas sensing performance by providing abundant pores, which facilitate the diffusion of gas molecules and enlarge the specific surface area, offering more active sites for gas

adsorption and reaction. This improves the kinetics of chemical reactions on the surface, leading to a good sensing performance.

The introduction of the Pt layer to ZnO structures to create FGFET devices for NO_2 sensing results in the formation of two critical energy or potential barriers that significantly impact the sensor's performance:

- Schottky barrier at the ZnO/Pt interface: This barrier arises due to the difference in work function between ZnO and Pt [29]. The Schottky barrier establishes a potential difference that influences charge carrier dynamics within the FGFET structure.
- Additional barrier due to NO_2 interaction: Upon the introduction of NO_2 gas, the molecules adsorb onto the ZnO surface, leading to an increase in electron depletion and the formation of an additional potential barrier.

These phenomena are theoretically substantiated and illustrated in Figures 7 and 8. Furthermore, the interplay between these two barriers results in a quantum well formation within the conductive channel of the FGFET. The band bending induced by the Schottky barrier, in conjunction with the electron depletion from NO_2 interaction, confines charge carriers within this quantum well. The confinement leads to enhanced charge carrier modulation, amplifying the sensitivity of the sensor to NO_2 gas concentrations. As a result, the conductive channel becomes significantly influenced by the concentration of NO_2, resulting in a robust sensing signal that accurately reflects environmental NO_2 levels, as seen in Figure 11b. The sensitivity magnitude increases with varying the gas concentration from 1 to 5 ppm in a linear fashion with good R-squared values. This linear dependence emphasizes the reliability of our sensors in detecting the oxidizing gas.

The limit of detection (LOD) for NO_2 was determined using the standard statistical method based on the signal-to-noise ratio, as defined by the following formula [30]:

$$\mathrm{LOD} = \frac{3\sigma}{\alpha} \tag{19}$$

where σ the standard deviation of the baseline signal (conductance in air) and α is the slope of the calibration curve obtained from the linear fit of sensor response versus NO_2 concentration. This approach ensures reliable estimation of the minimum detectable concentration with a 99% confidence level.

A limit of detection value as low as 1 ppm was obtained for the sensors where $\mathrm{LOD(R)} = 927$ ppb and $\mathrm{LOD(TR)} = 89$ ppb. These detectable NO_2 concentrations meet the Occupational Safety and Health Administration (OSHA) regulations, proving the devices' efficiency in indoor and environmental monitoring (The LOD values are below the short-term exposure limit STEL = 1 ppm). The TR architecture shows better reliability with 89 ppb as LOD which is less than 100 ppb, recognized as 1-h daily maximum concentrations of NO_2 (averaged over 3 years), according to National Ambient Air Quality Standards (NAAQS).

It is noteworthy to highlight that when compared to other studies on ZnO sensors and transistor-based sensors as listed in Table 1, our FGFET device demonstrates superior sensing performance. In another work [5], Andringa et al. demonstrated ZnO FETs operating at 200 °C with a detection limit of ~40 ppb NO_2 and response/recovery times of tens to a few hundred seconds. Their devices relied on gate biasing and exhibited incomplete recovery after NO_2 removal due to charge trapping at the ZnO/dielectric interface. By contrast, our floating-gate ZnO FETs operate without external gate bias, show stable recovery over repeated cycles, with quantum confinement effects further amplifying the response.

Table 1. Summary of previously reported metal oxide-based gas sensors and transistors to 5 ppm of NO_2.

Device Type	Substrate	Sensing Layer	Sensing Condition	Response	LOD (ppb)	References
Conductometric sensor	Alumina	ZnO thin film	400 °C	2.54 (1)	927	Present work
Resistive sensor	Alumina	ZnO film	250 °C	1.42 (2)	NA *	[31]
Resistive sensor	Glass	Ni-doped ZnO/PANi nanocomposite	RT **	0.14 (3)	NA	[32]
Resistive sensor	Alumina	ZnO	100 °C, under UV exposure	<1.5 (2)	NA	[33]
Resistive sensor	Alumina	Mg-doped ZnO	400 °C 30 °C, under UV exposure	1.01 (2) ≈1.5 (2)	NA NA	[34]
Resistive sensor	Alumina	ZnO	300 °C, under UV exposure	1.5 (2)	NA	[35]
Resistive sensor	NA	ZnO NPs decorated on CuO NWs	250 °C	1.17 (4)	NA	[36]
Resistive sensor	Oxidized Si substrate	ZnO nanosheets	RT, under UV exposure (1.2 mW/cm^2)	≈1.37 (2)	NA	[37]
Resistive sensor	Oxidized Si substrate	Au-functionalized ZnO nanosheets	RT, under UV exposure (0.35 mW/cm^2) RT, under UV exposure (1.2 mW/cm^2)	≈1.33 (2) ≈4.55 (2)	NA NA	[37]
Resistive sensor	Alumina	ZnO nanoneedles	195 °C	1.04 (5)	80	[38]
Resistive sensor	Alumina	ZnO Nanowires	250 °C	3.3 (2)	NA	[39]
Thin Film Transistor	Pt/Alumina	ZnO thin film	400 °C	11 (1)	89	Present work
Thin Film Transistor	SiO_2/Si	Indium Gallium Zinc Oxide thin film	RT	−0.998 (6)	100	[40]
Thin Film Transistor	Flexible Plastic Foil	Indium Gallium Zinc Oxide thin film	RT	<1.5 (7)	NA	[41]
Thin Film Transistor	SiO_2/Si	Indium Gallium Zinc Oxide thin film	100 °C	<4 (8)	NA	[42]
Thin Film Transistor	Silicon chip	ZnO nanowires	RT	1.088 (2)	NA	[43]
Organic Field Effect Transistor	BOPET	PCDTBT polymer	RT	≈0.5 (6)	1000	[44]

* NA: not available, ** RT: room temperature. (1) $S = \frac{G_{gas}-G_{air}}{G_{air}}$, (2) $S = \frac{R_{gas}}{R_{air}}$, (3) $S = \frac{R_{gas}-R_{air}}{R_{gas}}$, (4) $S = \frac{R_{air}}{R_{gas}}$, (5) $S = \frac{R_{gas}-R_{air}}{R_{air}}$, (6) $S = \frac{I_{gas}-I_{air}}{I_{air}}$, (7) $S = \frac{I_{air}}{I_{gas}}$, (8) $S = \frac{\frac{dlogI_{gas}}{dt}-\frac{dlogI_{air}}{dt}}{\frac{dlogI_{air}}{dt}}$.

While the highest response obtained for the FGFET sensor is 11 toward 5 ppm of NO_2, Pan et al. [43] initially achieved a low response of 1.088 for ZnO nanowires, which was enhanced to a comparable value of 12 using a more complex process to fabricate ZnO hierarchical nanostructures. Their method involved cleaning a silicon wafer with a pre-deposited silicon dioxide layer, spin-coating with photoresist, UV exposure and development, metal deposition, lift-off in acetone, and annealing at 700 °C to form Au nanoparticles. Zn powder was then vaporized and deposited in the presence of an oxygen-argon gas mixture. In contrast, we achieved nearly the same responsiveness using a

simpler and more scalable method. By sputtering thin films of Zn (200 nm) and Pt (100 nm) followed by thermal oxidation in air for 1 hour, we were able to produce a nanoporous structure with comparable sensitivity, making our process more suitable for large-scale and industrial applications.

The performance of the FGFET and resistor gas sensors is evaluated in terms of response and recovery times, which are critical parameters for gas sensing applications. Response and recovery times are defined as the time the sensor takes to reach a 90% and 90% change in the total conductance after gas injection and air injection, respectively.

Figure 12 shows the dynamic response-recovery curve of each sensor to 2 ppm NO_2 gas at the optimum temperature 400 °C. Since R sensor did not show full reversibility, it was not possible to calculate recovery at 90%.

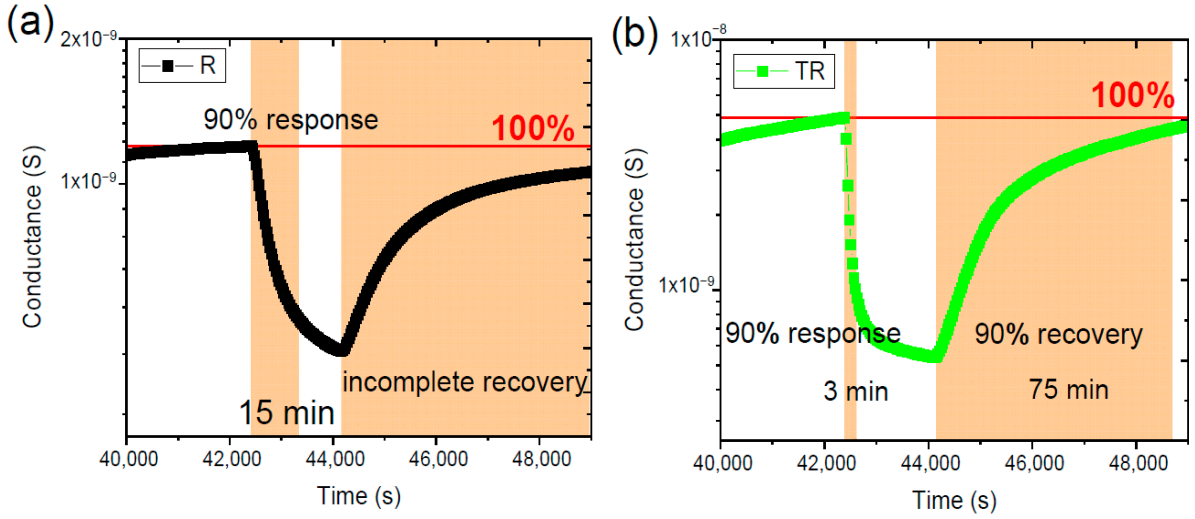


Figure 12. Dynamic response to 2 ppm NO_2 gas at 400 °C and 40% of relative humidity@20 °C for (**a**) resistor and (**b**) transistor devices.

TR presents shorter response/recovery time of 3/75 min, respectively, compared to the R sensor, which presents 15 min as response time and incomplete recovery. This is due to the enhanced sensing mechanism of the FGFET structure, by the confinement of the charge carrier in the conductive channel which can accelerate the catalytic activity of the sensor. It is worth noting that a chamber with 1L volume was used to locate the sensors. Using a 200 sccm flow it takes 5 min to completely fill and empty the chamber. Therefore, response and recovery times are limited by the volume of the chamber and in case of TR device may be significantly lower.

Besides that, NO_2 has strong adsorption to the surface due to the strong binding energy of NO_2 molecules and the difference in electron affinity between molecular oxygen (0.4 eV) and NO_2 (2.3 eV) which makes the recovery incomplete [12].

Repeatability in the context of gas sensing performance refers to the ability of a gas sensor to produce consistent and reliable results when exposed to the same concentration of a target gas under identical conditions over multiple tests. In other words, it measures the sensor's ability to reproduce the same output when the same conditions are applied repeatedly. In Figure 13, the dynamic response of R and TR sensors for 2 cycles is presented (the black line corresponds to the first cycle, while the red line represents the second cycle).

A cycle is defined as one complete air/NO_2 exposure/air purge sequence at fixed operating conditions (temperature, relative humidity, and a 1 V DC bias).

One can see the change in baseline conductance for R, accompanied by an increase in response for all concentrations in cycle 2. However, the baseline conductance is still constant for the TR device with a slight decrease in response.

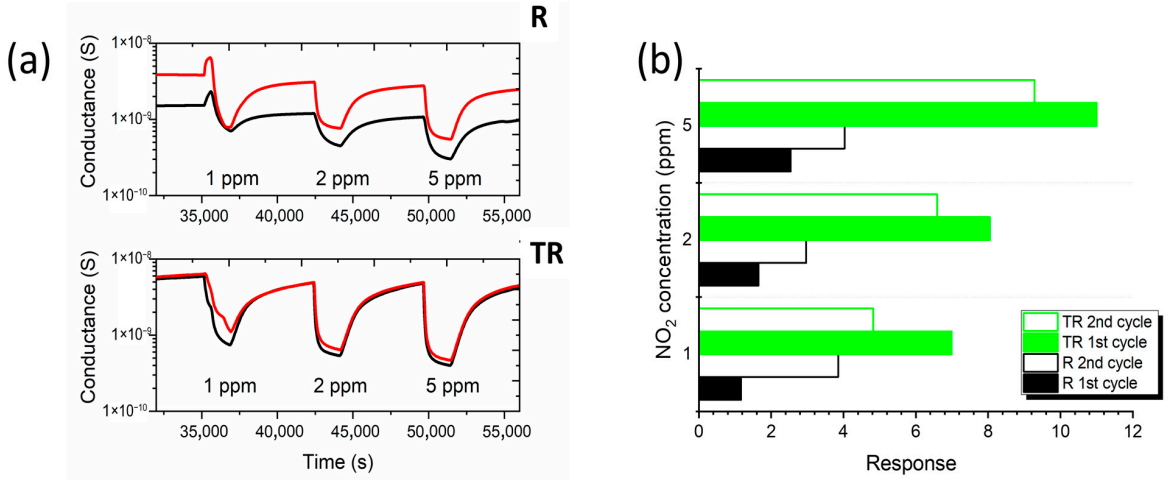


Figure 13. (**a**) Repeatability performance to NO_2 gas at 400 °C and 40% of relative humidity@20 °C: cycle 1 (black line) and cycle 2 (red line). (**b**) Histogram representation of sensitivity extracted from (**a**): filled rectangles and empty rectangles describe the first and second cycles, respectively.

Storage stability is among the important parameters that shape the sensing device's reliability. Figure 14 shows the response to 2 ppm of NO_2 at the same conditions over 37 days.

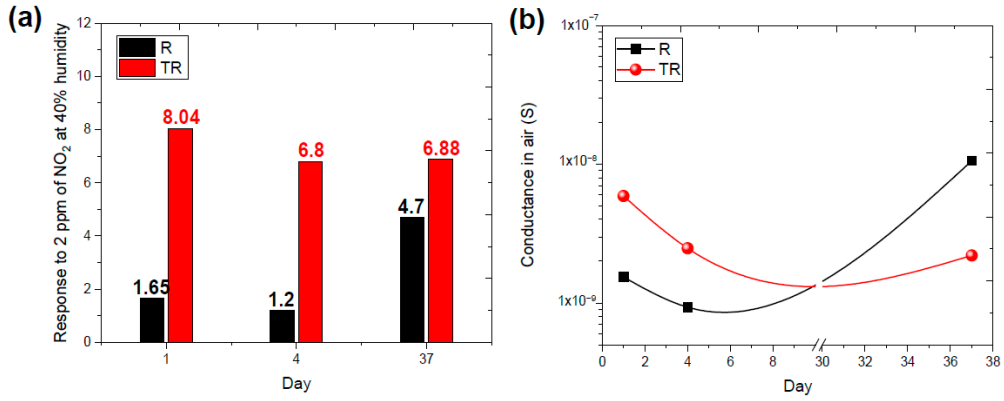


Figure 14. (**a**) Storage stability performance to 2 ppm NO_2 gas at 400 °C and 40% of relative humidity@20 °C. (**b**) Baseline conductance evolution of the sensors over 37 measurement days.

The sensors exhibit solid stability during the first three days, with R maintaining stability at around 73%, while TR shows even greater stability, holding steady at approximately 85%. The slight decrease in their responses over time may be attributed to the adsorption of atmospheric moisture, which can passivate active surface sites or alter the charge transfer dynamics at the ZnO interface. This phenomenon is consistent with observations reported by Sik Choi et al. [45], who found that the response of their sensors declined from 11.57 to 8.52 after three months of storage due to moisture uptake from the air.

Over prolonged storage in ambient atmosphere, ZnO transistor sensors often suffer from deteriorated response due to moisture and oxygen adsorption, defect-state formation, and carrier trapping. For example, Amna et al. [46] stated that in organic FET-based sensors, exposure to moisture/oxygen during idle periods causes trapping of mobile charges and shifts in threshold voltage, ultimately reducing the drain current and degrading response.

Similarly, studies on ZnO thin-film transistors show that oxygen molecules adsorbed onto surfaces or grain boundaries pull electrons from the conduction channel, increasing the depletion layer and raising baseline resistance (see Figure 14b); this effect reduces the

incremental modulation available when the device is exposed to NO_2 or other oxidizing gases [47].

However, the pronounced increase in R sensor response after 37 days of storage can be rationalized by considering the effect of long-term moisture adsorption. Previous thermogravimetric studies on tetrapod-shaped ZnO [48] have shown that, under humid conditions, water molecules gradually diffuse into surface cavities and grain boundaries, where they interact with lattice oxygen species to form hydroxyl groups upon heating. The extent of this uptake depends strongly on the relative humidity of the storage environment. During subsequent measurements at operating temperature, the presence of these hydroxyl species modifies the electronic landscape of the sensing film, leading to a shift in its baseline conductivity. In R device, this is manifested as a lower initial resistance before NO_2 exposure as shown in Figure 14b. The altered surface chemistry enhances the interaction between ZnO and NO_2 molecules, thereby amplifying the response after storage compared with the freshly fabricated sensor.

This interpretation is consistent with the notion that humidity-induced hydroxylation and related surface reconfiguration during storage can activate additional charge-transfer pathways, which become evident as improved sensitivity in later tests.

The different behaviors after storage of the R and TR sensors reflect the influence of device architecture: the TR sensor maintains stability due to channel-dominated operation [49], while the R sensor is directly governed by surface chemistry and defect dynamics, including oxygen vacancy redistribution. The prolonged storage in ambient laboratory conditions may lead to the formation or redistribution of intrinsic defects such as oxygen vacancies, which act as shallow donors in ZnO, thereby increasing the carrier concentration and conductivity with thermal processing [50].

Studying the humidity effect on gas sensing devices is crucial for ensuring their accuracy, reliability, and performance in real-world conditions. It provides valuable insights into how environmental factors influence sensor operation and helps in optimizing sensor design to handle varying humidity levels effectively. Figure 15 describes the gas response of R and TR gas sensors to 2 ppm NO_2 gas at 400 °C at different relative humidity.

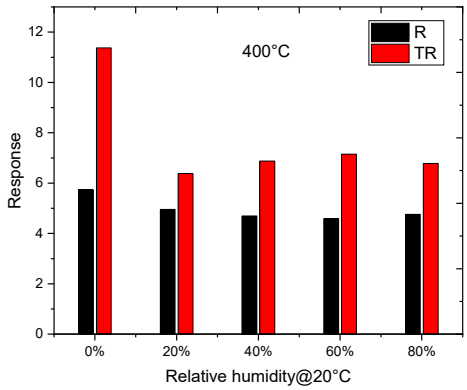


Figure 15. Response dependency on relative humidity levels at 400 °C, under exposure to 2 ppm NO_2.

As can be seen, the sensing response of the sensors exhibits the highest value in the dry environment and decreases with the presence of humidity, noting that transistors demonstrate better response compared to R sensor. This degradation in response is due to water molecules starting to occupy the sensor's active sites, reducing the availability for NO_2 adsorption [51]. The gas response of ZnO-based sensors to NO_2 clearly depends on humidity. For the R sensor, the response decreases from 5.73 in dry air (0% RH) to 4.76 at 80% RH, corresponding to a 17% reduction due to water molecules competing with NO_2

for adsorption sites and blocking reactive surface regions [52,53]. The TR sensor, while showing a higher dry response (11.37), drops more sharply to 6.78 at 80% RH, a reduction of ~40%, confirming its greater sensitivity to moisture interference.

Overall, the presence of water vapor in the environment can interfere with the adsorption of NO_2 molecules on the surface of ZnO, leading to a decrease in sensing response. Interestingly, as depicted in Figure 16, humidity has a beneficial impact on sensor performance, particularly in terms of recovery. The recovery is improved under humid air for all devices where TR presents full recovery at higher humidity levels (60% and 80%). This complete recovery of ZnO upon increasing humidity is primarily due to the hydration of the surface and the subsequent desorption of adsorbed gas. Water vapor interacts with the ZnO surface, displacing target gases like NO_2, and cleansing the surface.

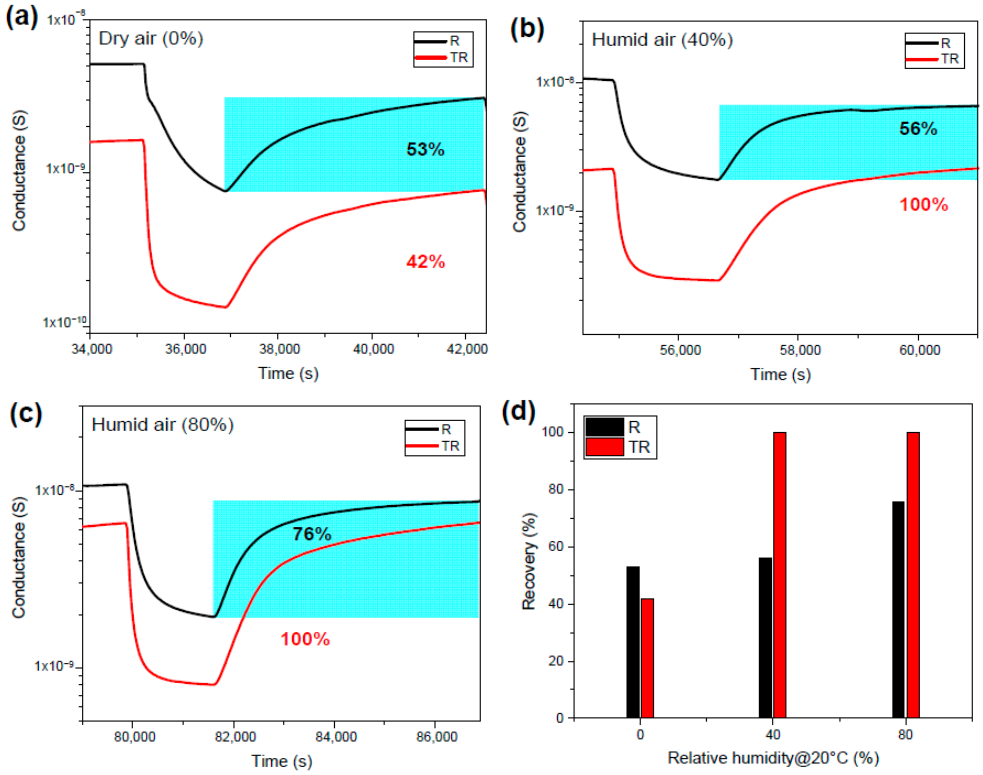


Figure 16. Dynamic response-recovery curves to 2 ppm in dry (**a**) and humid (**b**–**c**) environments with (**d**) representative histogram of recovery dependency on humidity levels at 400 °C.

Other metal–oxide FET sensors have also been explored for NO_2 detection. For instance, In_2O_3-based transistors have achieved sub-ppb detection limits (~0.27 ppb) with rapid response and recovery at relatively low temperatures (75 °C), highlighting their excellent properties when gate bias is optimized [54]. Likewise, WO_3 FET employing horizontal floating-gate architecture uses charge-storage engineering to improve recovery and enhance discrimination against interfering gases [6]. Shin et al. have studied FGFET by applying an "erase" bias ($\Delta V = -2$ V) to store excess holes in the floating gate, which raises the electron concentration at the WO_3/passivation layer interface. This modulation leads to a 2.4 times larger change in voltage and a 3.2 times increase in sensitivity to NO_2 compared to the non-engineered state. Also, recovery speed was improved by applying a pre-bias greater than the read bias. The study explains the enhanced response, sensitivity, and recovery using energy band diagrams, showing how the stored charge increases the density of carriers available for interaction with NO_2 molecules, thus amplifying the sensing performance. Compared with these devices, our floating-gate ZnO FET operates without external gate bias, achieves stable recovery and good selectivity under varying

humidity, and maintains enhanced sensitivity even after 37 days of storage, confirming its competitiveness among state-of-the-art MOX-FET gas sensors.

In the field of gas sensing, selectivity refers to the sensor's ability to preferentially detect a specific target gas in the presence of other gases. A highly selective sensor responds primarily to the target gas with minimal interference or response to other gases in the environment. This property is crucial for accurate detection, as it ensures that the sensor can distinguish the target gas from potentially similar gases or background substances, leading to more reliable and precise measurements. To examine this parameter, we measure the sensitivity of our sensors to different gases shown in Figure 17. As can be seen, TR presents higher selectivity performance than R sensor, which shows very poor selectivity by exhibiting nearly identical responses toward ammonia, ethanol, hydrogen, and nitrogen dioxide.

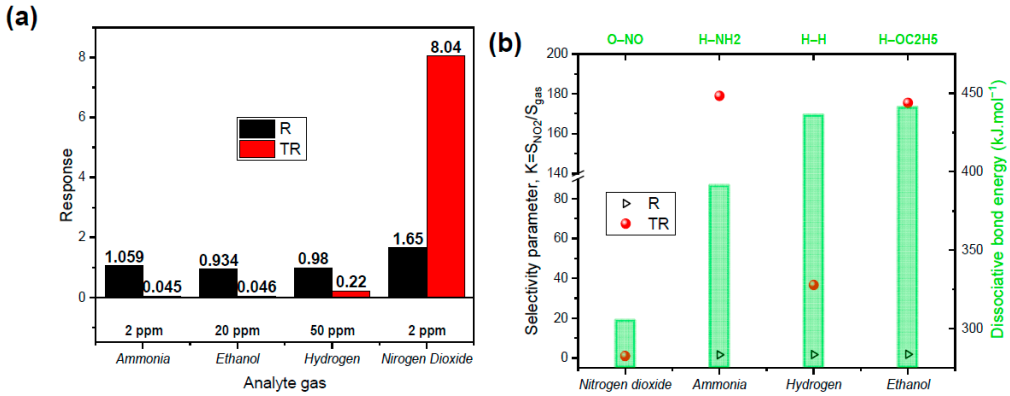


Figure 17. (**a**) Gas response of the ZnO sensor at 400 °C and 40% RH. Responses were recorded at the concentrations indicated in the legend. (**b**) Selectivity factor, defined as the response to each gas normalized to the response to NO_2. Empty triangles correspond to the R sensor, while red circles represent the TR sensor. The bond-dissociation energy values for the relevant bonds are represented as green histograms for comparison.

The selectivity parameters $K = \frac{S_{gas}}{S_{NO_2}}$ for our sensors (R, TR) reveal significant differences in their ability to preferentially detect NO_2 compared to the other gases. For R sensor, the selectivity values indicate that it has a moderate preference for NO_2 over ammonia (K = 1.56), ethanol (K = 1.77), and hydrogen (K = 1.69) but the selectivity is not particularly high. In contrast, TR shows exceptionally high selectivity towards NO_2 when compared to ammonia and ethanol, with values of 179 and 175, respectively. This indicates a remarkable ability of TR to distinguish NO_2 from these gases. In general, the selectivity to NO_2 is attributed not only to the high concentration of electron donor sites in the metal oxide [55] and the high electron affinity of NO_2, which enables it to effectively withdraw electrons from ZnO and strongly modulate its conductivity, but also to thermodynamic factors related to the low bond dissociation energy of NO_2 molecules (see Figure 17b). NO_2 molecules possess a relatively low bond dissociation energy (305 kJ/mol), significantly lower than that of common interfering gases such as H_2 (436 kJ/mol), NH_3 (391 kJ/mol), and ethanol (441 kJ/mol). This means the oxidizing molecules can more readily dissociate and interact with the sensor surface, facilitating efficient adsorption and reaction [56].

5. Conclusions

FET architecture significantly enhances sensitivity, selectivity, stability, and response speed. Both simulation and experimental results confirm that the FET benefits from intrinsic electron confinement and quantum well effects, which amplify the sensing response even without external gate biasing. Moreover, the FET exhibits strong resilience under

varying environmental conditions, including changes in humidity, making it a promising candidate for real-world applications such as urban air-quality monitoring, industrial safety, vehicle emission control, and personal exposure assessment. While the relatively high operating temperature may limit scalability due to power and heating requirements, it remains essential for achieving reliable NO_2 detection. Future efforts will therefore focus on reducing this constraint through material modification or micro-hotplate integration, paving the way toward next-generation gas sensors that combine high performance with operational simplicity and low power demand.

Author Contributions: Conceptualization, H.H.; methodology, H.H. and H.P.; software, H.H. and Z.B.; validation, D.Z., E.C. and Z.B.; formal analysis, H.H. and M.B.A.; investigation, H.H.; resources, D.Z., E.C. and Z.B.; data curation, H.H. and M.B.A.; writing—original draft preparation, H.H.; writing—review and editing, M.B.A., H.P. and D.Z.; visualization, H.H.; supervision, D.Z. and E.C.; project administration, E.C.; funding acquisition, E.C. All authors have read and agreed to the published version of the manuscript.

Funding: This research was funded by M.U.R. under grant PRIN 2022RWYH2K "Sarcopenia-on-chip: an integrated platform based on chemical sensors, microfluidic devices, and machine learning algorithms for the development and testing of personalized treatment for sarcopenia disease (SELENE)".

Institutional Review Board Statement: Not applicable.

Informed Consent Statement: Informed consent was obtained from all subjects involved in the study.

Data Availability Statement: The original contributions presented in this study are included in the article. Further inquiries can be directed to the corresponding author.

Conflicts of Interest: The authors declare no conflicts of interest.

References

1. Khorramifar, A.; Karami, H.; Lvova, L.; Kolouri, A.; Łazuka, E.; Piłat-Rożek, M.; Łagód, G.; Ramos, J.; Lozano, J.; Kaveh, M.; et al. Environmental Engineering Applications of Electronic Nose Systems Based on MOX Gas Sensors. *Sensors* **2023**, *23*, 5716. [CrossRef]
2. Gong, H.; Hu, J.; Wang, J.; Ong, C.; Zhu, F. Nano-crystalline Cu-doped ZnO thin film gas sensor for CO. *Sens. Actuators B Chem.* **2006**, *115*, 247–251. [CrossRef]
3. Ismail, B.; Abaab, M.; Rezig, B. Structural and electrical properties of ZnO films prepared by screen printing technique. *Thin Solid Film.* **2001**, *383*, 92–94. [CrossRef]
4. Shin, H.; Park, J.; Kim, D.; Choi, K.; Park, M.-K.; Hwang, J.; Lee, S.; Joo, Y.-C.; Jung, G.; Lee, J.-H. Optimization of co-sputtered zinc indium tin oxide-based MOSFET-type sensor for effective NO_2 gas detection. *Sens. Actuators B Chem.* **2025**, *428*, 137262. [CrossRef]
5. Andringa, A.-M.; Piliego, C.; Katsouras, I.; Blom, P.W.M.; Leeuw, D.M.D. NO_2 Detection and Real-Time Sensing with Field-Effect Transistors. *Chem. Mater.* **2014**, *26*, 773–785. [CrossRef]
6. Shin, W.; Hong, S.; Jeong, Y.; Jung, G.; Park, J.; Kim, D.; Lee, C.; Park, B.-G.; Lee, J.-H. Effect of charge storage engineering on the NO_2 gas sensing properties of a WO_3 FET-type gas sensor with a horizontal floating-gate. *Nanoscale* **2021**, *13*, 9009–9017. [CrossRef]
7. Lee, J.-H. Gas sensors using hierarchical and hollow oxide nanostructures: Overview. *Sens. Actuators B Chem.* **2009**, *140*, 319–336. [CrossRef]
8. Yamazoe, N.; Shimanoe, K. Roles of shape and size of component crystals in semiconductor gas sensors: I. Response to oxygen. *J. Electrochem. Soc.* **2008**, *155*, J85. [CrossRef]
9. Nagarjuna, Y.; Hsiao, Y.-J.; Wang, S.-C.; Shao, C.-Y.; Huang, Y.-C. Nanoporous ZnO structure prepared by HiPIMS sputtering for enhanced ozone gas detection. *Mater. Today Commun.* **2023**, *35*, 106024. [CrossRef]
10. Pleshek, D.; Tran, J.; Li, Y.; Shirani, A.; Shevchenko, E.V.; Berman, D. Swelling-assisted sequential infiltration synthesis of nanoporous ZnO films with highly accessible pores and their sensing potential for ethanol. *ACS Appl. Mater. Interfaces* **2021**, *13*, 35941–35948. [CrossRef]
11. Han, S.; Huang, W.; Shi, W.; Yu, J. Performance improvement of organic field-effect transistor ammonia gas sensor using ZnO/PMMA hybrid as dielectric layer. *Sens. Actuators B Chem.* **2014**, *203*, 9–16. [CrossRef]

12. Arbia, M.B.; Kim, S.-H.; Yoon, J.-B.; Comini, E. Preparation of NiO NWs by Thermal Oxidation for Highly Selective Gas-Sensing Applications. *Sensors* **2025**, *25*, 2075. [CrossRef]
13. Li, M.; Li, B.; Meng, F.; Liu, J.; Yuan, Z.; Wang, C.; Liu, J. Highly sensitive and selective butanol sensors using the intermediate state nanocomposites converted from β-FeOOH to α-Fe_2O_3. *Sens. Actuators B Chem.* **2018**, *273*, 543–551. [CrossRef]
14. Zhang, K.; Qin, S.; Tang, P.; Feng, Y.; Li, D. Ultra-sensitive ethanol gas sensors based on nanosheet-assembled hierarchical ZnO-In_2O_3 heterostructures. *J. Hazard. Mater.* **2020**, *391*, 122191. [CrossRef]
15. Chen, M.; Wang, Z.; Han, D.; Gu, F.; Guo, G. High-sensitivity NO_2 gas sensors based on flower-like and tube-like ZnO nanomaterials. *Sens. Actuators B Chem.* **2011**, *157*, 565–574. [CrossRef]
16. Qin, W.; Yuan, Z.; Gao, H.; Zhang, R.; Meng, F. Perovskite-structured $LaCoO_3$ modified ZnO gas sensor and investigation on its gas sensing mechanism by first principle. *Sens. Actuators B Chem.* **2021**, *341*, 130015. [CrossRef]
17. Gurylev, V.; Perng, T.P. Defect engineering of ZnO: Review on oxygen and zinc vacancies. *J. Eur. Ceram. Soc.* **2021**, *41*, 4977–4996. [CrossRef]
18. Sonker, R.K.; Sabhajeet, S.; Singh, S.; Yadav, B. Synthesis of ZnO nanopetals and its application as NO_2 gas sensor. *Mater. Lett.* **2015**, *152*, 189–191. [CrossRef]
19. Kumar, R.R.; Murugesan, T.; Dash, A.; Hsu, C.-H.; Gupta, S.; Manikandan, A.; Kumar Anbalagan, A.; Lee, C.-H.; Tai, N.-H.; Chueh, Y.-L. Ultrasensitive and light-activated NO_2 gas sensor based on networked MoS_2/ZnO nanohybrid with adsorption/desorption kinetics study. *Appl. Surf. Sci.* **2021**, *536*, 147933. [CrossRef]
20. Yang, Z.; Jiang, L.; Wang, J.; Liu, F.; He, J.; Liu, A.; Lv, S.; You, R.; Yan, X.; Sun, P. Flexible resistive NO_2 gas sensor of three-dimensional crumpled MXene Ti_3C_2Tx/ZnO spheres for room temperature application. *Sens. Actuators B Chem.* **2021**, *326*, 128828. [CrossRef]
21. Li, J.; Cai, C.; Li, Z.-H. Knudsen diffusion differs from Fickian diffusion. *Phys. Fluids* **2021**, *33*, 042009. [CrossRef]
22. Luo, Y.; Gao, J.; Fu, H.; Liu, S.; Hua, Z. A selective methane gas sensor based on SnO_2 utilizing a reactive and porous substrate. *Chin. J. Anal. Chem.* **2025**, *53*, 100526. [CrossRef]
23. Sakai, G.; Matsunaga, N.; Shimanoe, K.; Yamazoe, N. Theory of gas-diffusion controlled sensitivity for thin film semiconductor gas sensor. *Sens. Actuators B Chem.* **2001**, *80*, 125–131. [CrossRef]
24. Arbia, M.B.; Helal, H.; Saidi, F.; Maaref, H. Investigation of 1.9 µm GINA Simulated as Intrinsic Layer in a GaAs Homojunction: From 25% Towards 32.4% Conversion Yield. *J. Electron. Mater.* **2020**, *49*, 6308–6316. [CrossRef]
25. Silvaco International. *ATLAS User's Manual a 2D Numerical Device Simulator, 2004*; Silvaco Int.: Santa Clara, CA, USA, 2016.
26. Yang, G.W.; Seo, S.G.; Choi, S.; Kim, D.H.; Jin, S.H. Unscrambling for subgap density-of-states in multilayered MoS_2 field effect transistors under DC bias stress via optical charge-pumping capacitance-voltage spectroscopy. *IEEE Access* **2021**, *9*, 73090–73102. [CrossRef]
27. De, A.; Karmakar, A.; Ghosh, R.; Saha, P. (Eds.) Investigation of MoS_2 based dual gate MOSFET as a H_2 sensor considering catalytic metal gate approach. In *2022 IEEE VLSI Device Circuit and System (VLSI DCS)*; IEEE: New York, NY, USA, 2022.
28. Choi, S.; Seo, S.G.; Yu, H.R.; Kim, S.Y.; Kim, D.H.; Jin, S.H. Hydrophobic Polymer Encapsulation Effects on Subgap Density of States in Multilayered Molybdenum Disulfide Field—Effect Transistors. *Phys. Status Solidi (RRL)-Rapid Res. Lett.* **2020**, *14*, 1900492. [CrossRef]
29. Chirakkara, S.; Choudhury, P.R.; Nanda, K.K.; Krupanidhi, S.B. Understanding Pt–ZnO:In Schottky nanocontacts by conductive atomic force microscopy. *Mater. Res. Express* **2016**, *3*, 045023. [CrossRef]
30. Franco, M.A.; Conti, P.P.; Andre, R.S.; Correa, D.S. A review on chemiresistive ZnO gas sensors. *Sens. Actuators Rep.* **2022**, *4*, 100100. [CrossRef]
31. Modak, M.; Mahajan, S.; Shinde, M.; Rane, S.; Jagtap, S. Sensitive, selective and low detection limit of NO_2 gas sensor based on Cu/ZnO/rGO nanocomposites. *J. Mater. Sci. Mater. Electron.* **2022**, *33*, 26205–26224. [CrossRef]
32. Jain, S.; Karmakar, N.; Shah, A.; Shimpi, N.G. Development of Ni doped ZnO/polyaniline nanocomposites as high response room temperature NO_2 sensor. *Mater. Sci. Eng. B* **2019**, *247*, 114381. [CrossRef]
33. Hjiri, M.; Alkaoud, A.; Neri, G. Low operating temperature of UV photo-activated In-doped ZnO NO_2 sensors. *Appl. Phys. A* **2023**, *129*, 861. [CrossRef]
34. Jaballah, S.; Hjiri, M.; Zahmouli, N.; Albargi, H.B.; Dhahri, R.; Dahman, H.; Mir, L.E.; Neri, G. Room temperature UV-Vis activated NO_2 gas sensor-based Mg-doped zinc oxide nanopowders. *J. Mater. Sci. Mater. Electron.* **2023**, *34*, 137. [CrossRef]
35. Hjiri, M.; Neri, G. Photo-Activated Ga-ZnO Gas Sensor for NO_2 Detection at Near Ambient Temperature. *J. Inorg. Organomet. Polym. Mater.* **2023**, *34*, 3374–3383. [CrossRef]
36. Han, T.-H.; Bak, S.-Y.; Kim, S.; Lee, S.H.; Han, Y.-J.; Yi, M. Decoration of CuO NWs Gas Sensor with ZnO NPs for Improving NO_2 Sensing Characteristics. *Sensors* **2021**, *21*, 2103. [CrossRef]
37. Mun, Y.; Park, S.; An, S.; Lee, C.; Kim, H.W. NO_2 gas sensing properties of Au-functionalized porous ZnO nanosheets enhanced by UV irradiation. *Ceram. Int.* **2013**, *39*, 8615–8622. [CrossRef]

38. Gonzalez-Chavarri, J.; Parellada-Monreal, L.; Castro-Hurtado, I.; Castaño, E.; Mandayo, G.G. ZnO nanoneedles grown on chip for selective NO_2 detection indoors. *Sens. Actuators B Chem.* **2018**, *255*, 1244–1253. [CrossRef]
39. Chen, X.; Shen, Y.; Zhang, W.; Zhang, J.; Wei, D.; Lu, R.; Zhu, L.; Li, H.; Shen, Y. In-situ growth of ZnO nanowire arrays on the sensing electrode via a facile hydrothermal route for high-performance NO_2 sensor. *Appl. Surf. Sci.* **2018**, *435*, 1096–1104. [CrossRef]
40. Vijjapu, M.T.; Surya, S.G.; Yuvaraja, S.; Zhang, X.; Alshareef, H.N.; Salama, K.N. Fully Integrated Indium Gallium Zinc Oxide NO_2 Gas Detector. *ACS Sens.* **2020**, *5*, 984–993. [CrossRef]
41. Knobelspies, S.; Bierer, B.; Daus, A.; Takabayashi, A.; Salvatore, G.A.; Cantarella, G.; Ortiz Perez, A.; Wöllenstein, J.; Palzer, S.; Tröster, G. Photo-Induced Room-Temperature Gas Sensing with a-IGZO Based Thin-Film Transistors Fabricated on Flexible Plastic Foil. *Sensors* **2018**, *18*, 358. [CrossRef]
42. Kim, K.S.; Ahn, C.H.; Jung, S.H.; Cho, S.W.; Cho, H.K. Toward Adequate Operation of Amorphous Oxide Thin-Film Transistors for Low-Concentration Gas Detection. *ACS Appl. Mater. Interfaces* **2018**, *10*, 10185–10193. [CrossRef] [PubMed]
43. Pan, X.; Zhao, X.; Chen, J.; Bermak, A.; Fan, Z. A fast-response/recovery ZnO hierarchical nanostructure based gas sensor with ultra-high room-temperature output response. *Sens. Actuators B Chem.* **2015**, *206*, 764–771. [CrossRef]
44. Kumar, A.; Jha, P.; Singh, A.; Chauhan, A.K.; Gupta, S.K.; Aswal, D.K.; Muthe, K.P.; Gadkari, S.C. Modeling of gate bias controlled NO_2 response of the PCDTBT based organic field effect transistor. *Chem. Phys. Lett.* **2018**, *698*, 7–10. [CrossRef]
45. Sik Choi, M.; Young Kim, M.; Mirzaei, A.; Kim, H.-S.; Kim, S.-i.; Baek, S.-H.; Won Chun, D.; Jin, C.; Hyoung Lee, K. Selective, sensitive, and stable NO_2 gas sensor based on porous ZnO nanosheets. *Appl. Surf. Sci.* **2021**, *568*, 150910. [CrossRef]
46. Amna, B.; Ozturk, T. Organic field-effect transistor-based sensors: Recent progress, challenges and future outlook. *J. Mater. Chem. C* **2025**, *13*, 8354–8424. [CrossRef]
47. Khan, N.D. An Investigation of the Performance and Stability of Zinc Oxide Thin-Film Transistors and the Role of High-k Dielectrics. Ph.D. Thesis, De Montfort University, Leicester, UK, 2010.
48. Bai, Z.; Xie, C.; Hu, M.; Zhang, S.; Zeng, D. Effect of humidity on the gas sensing property of the tetrapod-shaped ZnO nanopowder sensor. *Mater. Sci. Eng. B* **2008**, *149*, 12–17. [CrossRef]
49. Shin, W.; Jung, G.; Hong, S.; Jeong, Y.; Park, J.; Kim, D.; Jang, D.; Kwon, D.; Bae, J.-H.; Park, B.-G.; et al. Proposition of deposition and bias conditions for optimal signal-to-noise-ratio in resistor- and FET-type gas sensors. *Nanoscale* **2020**, *12*, 19768–19775. [CrossRef]
50. Feng, W.-W.; Cho, S.; Wang, M.-S.; Dung, D.D. Co-contribution of hydrogen impurities and native defects might be the answer for the n-type conductivity in ZnO. *Phys. Lett. A* **2016**, *380*, 480–484. [CrossRef]
51. Wang, J.; Shen, Y.; Li, X.; Xia, Y.; Yang, C. Synergistic effects of UV activation and surface oxygen vacancies on the room-temperature NO_2 gas sensing performance of ZnO nanowires. *Sens. Actuators B Chem.* **2019**, *298*, 126858. [CrossRef]
52. Ben Arbia, M.; Helal, H.; Comini, E. Recent Advances in Low-Dimensional Metal Oxides via Sol-Gel Method for Gas Detection. *Nanomaterials* **2024**, *14*, 359. [CrossRef]
53. Kaneti, Y.V.; Yue, J.; Jiang, X.; Yu, A. Controllable synthesis of ZnO nanoflakes with exposed (1010) for enhanced gas sensing performance. *J. Phys. Chem. C* **2013**, *117*, 13153–13162. [CrossRef]
54. Yeom, G.; Kwon, D.; Shin, W.; Park, M.-K.; Kim, J.-J.; Lee, J.-H. Fast-response/recovery In_2O_3 thin-film transistor-type NO_2 gas sensor with floating-gate at low temperature. *Sens. Actuators B Chem.* **2023**, *394*, 134477. [CrossRef]
55. Marikutsa, A.; Rumyantseva, M.; Konstantinova, E.A.; Gaskov, A. The Key Role of Active Sites in the Development of Selective Metal Oxide Sensor Materials. *Sensors* **2021**, *21*, 2554. [CrossRef] [PubMed]
56. Pakdel, H.; Borsi, M.; Ponzoni, M.; Comini, E. Enhanced Gas Sensing Performance of CuO-ZnO Composite Nanostructures for Low-Concentration NO_2 Detection. *Chemosensors* **2024**, *12*, 54. [CrossRef]

Disclaimer/Publisher's Note: The statements, opinions and data contained in all publications are solely those of the individual author(s) and contributor(s) and not of MDPI and/or the editor(s). MDPI and/or the editor(s) disclaim responsibility for any injury to people or property resulting from any ideas, methods, instructions or products referred to in the content.